

Article

Enhanced Photocatalytic and Anticancer Activity of Zn-Doped BaTiO₃ Nanoparticles Prepared through a Green Approach Using Banana Peel Extract

Maqusood Ahamed ^{1,*}  and M. A. Majeed Khan ²¹ Department of Physics and Astronomy, College of Science, King Saud University, Riyadh 11451, Saudi Arabia² College of Science, King Saud University, Riyadh 11451, Saudi Arabia; mmkhan@ksu.edu.sa

* Correspondence: mahamed@ksu.edu.sa

Abstract: Perovskite barium titanate (BaTiO₃) has received a lot of interest due to its extraordinary dielectric and ferroelectric properties, along with its moderate biocompatibility. Here, we investigated how Zn doping tuned the physicochemical characteristics, photocatalytic activity, and anticancer potential of BaTiO₃ nanoparticles synthesized from banana peel extract. XRD, TEM, SEM, EDS, XPS, BET, Raman, and PL were utilized to characterize the as-synthesized pure and Zn (1 and 3 mol%)-doped BaTiO₃ nanoparticles. All of the synthesized samples showed evidence of the BaTiO₃ tetragonal phase, and the XRD patterns of the Zn-doped BaTiO₃ nanoparticles showed the presence of a Zn peak. The particle size of BaTiO₃ decreased with increasing levels of Zn doping without morphological changes. After Zn doping, the PL intensity of BaTiO₃ decreased, suggesting a lower electron–hole recombination rate. BET analysis found that the surface area of Zn-doped BaTiO₃ nanoparticles was higher than that of pure BaTiO₃. Under visible irradiation, the photocatalytic activity of pure and Zn-doped BaTiO₃ nanoparticles was compared, and a remarkable 85% photocatalytic activity of Zn (3%)-doped BaTiO₃ nanoparticles was measured. As a result, Zn-doped BaTiO₃ nanoparticles are recognized as excellent photocatalysts for degrading organic pollutants. According to cytotoxicity data, Zn (3%)-doped BaTiO₃ nanoparticles display four-fold greater anticancer activity against human lung carcinoma (A549) than pure BaTiO₃ nanoparticles. It was also observed that Zn-doped BaTiO₃ nanoparticles kill cancer cells by increasing the intracellular level of reactive oxygen species. Furthermore, compared to pure BaTiO₃, the Zn-doped BaTiO₃ nanostructure showed better cytocompatibility in non-cancerous human lung fibroblasts (IMR90). The Zn-doped BaTiO₃ nanoparticles have a reduced particle size, increased surface area, and a lower electron–hole recombination rate, which are highly beneficial for enhanced photocatalytic and anticancer activity. Overall, current data showed that green-fabricated Zn-BaTiO₃ nanoparticles have superior photocatalytic and anticancer effects along with improved biocompatibility compared to those of pure BaTiO₃. This work underlines the significance of utilizing agricultural waste (e.g., fruit peel) for the fabrication of BaTiO₃-based nanostructures, which hold great promise for biomedical and environmental applications.

Keywords: perovskite BaTiO₃; Zn doping; eco-friendly synthesis; photocatalysis; cytotoxicity; biocompatibility



Citation: Ahamed, M.; Khan, M.A.M. Enhanced Photocatalytic and Anticancer Activity of Zn-Doped BaTiO₃ Nanoparticles Prepared through a Green Approach Using Banana Peel Extract. *Catalysts* **2023**, *13*, 985. <https://doi.org/10.3390/catal13060985>

Academic Editors: Tamás Gyulavári, Klára Hernádi and Zsolt Pap

Received: 5 May 2023

Revised: 29 May 2023

Accepted: 30 May 2023

Published: 8 June 2023



Copyright: © 2023 by the authors. Licensee MDPI, Basel, Switzerland. This article is an open access article distributed under the terms and conditions of the Creative Commons Attribution (CC BY) license (<https://creativecommons.org/licenses/by/4.0/>).

1. Introduction

Nanoscale barium titanate (BaTiO₃) is a remarkable perovskite-type material that exhibits exceptional dielectric and ferroelectric properties [1,2]. BaTiO₃ nanoparticles find extensive usage in various technological applications, including transducers, infrared detectors, electromechanical devices, actuators, multilayer capacitors, and electro-optical devices [3,4]. Additionally, BaTiO₃ nanoparticles exhibit promising potential for biomedical applications such as drug delivery, tissue engineering, and cancer therapy [5,6].

Different crystallographic phases exist for BaTiO₃, with cubic and tetragonal phases being the most stable [2]. The effectiveness of a semiconductor photocatalyst depends on a number of factors, such as band gap, light absorption, charge carrier recombination rate, crystal orientation, morphology, and particle size [7,8]. The preparation of a photocatalyst that operates in visible light is typically accomplished by doping a semiconductor with an appropriate metal element [9]. Recent studies of metal ion-doped oxide semiconductor nanoparticles have gained attention due to the fact that the presence of metal ions in oxide semiconductors (e.g., BaTiO₃) results in a narrow band gap, high visible light absorption, and a low recombination rate of electron–hole pairs [10].

The catalytic efficiency of BaTiO₃ could be significantly improved by doping it with metal ions (e.g., Zn²⁺) [11]. Metal ion doping causes a narrow bandgap and a diminishing electron–hole recombination rate in BaTiO₃ nanoparticles [12]. Hence, tuning the physico-chemical properties of BaTiO₃ via metal ion doping can be a promising tool for their use in photocatalysis and anticancer activity [6]. Pure and metal-doped BaTiO₃ nanoparticles can be synthesized using a variety of physical and chemical methods. However, physical methods are expensive, energy-intensive, and temperature-dependent, and chemical approaches often result in the release of harmful chemicals into the environment [13]. Furthermore, chemical and physical routes for the synthesis of nanostructures are not suitable for biomedical applications [14]. Currently, eco-friendly green methods are being applied to synthesize semiconductor nanoparticles because of the benefits they provide in terms of particle homogeneity, crystallinity, particle size distribution, processing ease, cost effectiveness, and sustainability [15].

Here, we developed a facile, low-cost, and environmentally friendly approach for the synthesis of pure and Zn (1 and 3 mol%)-doped BaTiO₃ nanoparticles from banana peel extract. Banana peel contains several health-beneficial phytochemicals [16]. The compounds derived from banana peel extract were used in the green synthesis of both pristine and Zn-doped BaTiO₃ nanoparticles as reducing and stabilizing agents. Banana peel has excellent antioxidant, antimicrobial, and antibiotic properties due to its high concentration of phenolic compounds and dietary fibers [17]. The high concentration of flavonoids found in banana peel has been observed to possess anticancer properties [18]. The aim of this research was to integrate the advantageous properties of Zn and BaTiO₃, provided by banana peel extract, in order to augment the photocatalytic and anticancer effect. Prepared pure and Zn-doped BaTiO₃ nanoparticles were characterized via field emission transmission electron microscopy (FETEM), energy-dispersive spectroscopy (EDS), field emission scanning electron microscopy (FESEM), X-ray diffraction (XRD), X-ray photoelectron spectroscopy (XPS), Brunauer–Emmett–Teller (BET) analysis, Raman, and photoluminescence (PL) spectroscopy. Synthesized nanoparticles were assessed for their photocatalytic activity against methylene blue (MB) dye under visible light. Human lung cancer (A549) cells were used to examine the anticancer potential of the as-synthesized pure and Zn-doped BaTiO₃ nanoparticles. Reactive oxygen species (ROS) were investigated to delineate the plausible mechanism of the anticancer activity of the synthesized samples. Human lung fibroblast (IMR90) cells were used to determine the cytocompatibility of the prepared nanoparticles.

2. Results and Discussion

2.1. XRD Analysis

In Figure 1A, the XRD patterns in the 2θ range of 20–90 degrees demonstrate the phase structure of the pure and Zn-doped BaTiO₃ nanoparticles. Main diffraction peaks of pure BaTiO₃ nanoparticles are found at 2θ values of 22.39, 31.39, 39.14, 45.38, 51.11, 56.40, 66.07, 70.67, 75.04, 79.39, and 83.76, corresponding to the (100), (110), (111), (200), (210), (211), (220), (221), (310), (311), and (320) crystal planes of tetragonal-phase BaTiO₃ (JCPDS no. 05-0626) (Khan et al., 2021b). All of the above-mentioned peaks were also seen in Zn (1 and 3%)-doped BaTiO₃ nanostructures, as was an additional peak at 43.33° that matched the (101) crystal plane of the face-centered cubic phase of Zn (JCPDS no. 004-0831) [19]. Both

the pure and Zn-doped BaTiO₃ nanostructures lacked any peaks indicative of impurities. Scherrer's equation was used to calculate the average particle size [20]. Pure and Zn (1 and 3 mol%)-doped nanoparticles have crystallite sizes of 57.4, 48.5, and 35.2 nm, respectively. A very prevalent pattern that was also mentioned in our earlier work is the reduction in particle size following metal ion doping [21]. The substitution of Zn²⁺ for Ba²⁺ in the BaTiO₃ crystalline structure is responsible for the reduction in the particle size of the doped BaTiO₃ in comparison to that of the pure BaTiO₃. This might be because Zn²⁺ ions have a smaller ionic radius (74 pm) than does Ba²⁺ (135 pm). Furthermore, we found that the XRD peak (111) in the Zn-doped BaTiO₃ nanostructures slightly shifted to a lower value compared to that of the pure BaTiO₃ (Figure 1B). In the context of lattice strain, a peak shift toward a lower value suggests lattice expansion. Lattice strain refers to the deformation of a crystal lattice from its ideal structure. It can result from various factors, including mechanical stress, the presence of impurities (e.g., via doping), or crystal defects. The peak shift is further evidence of the integration of Zn ions in BaTiO₃ nanoparticles.

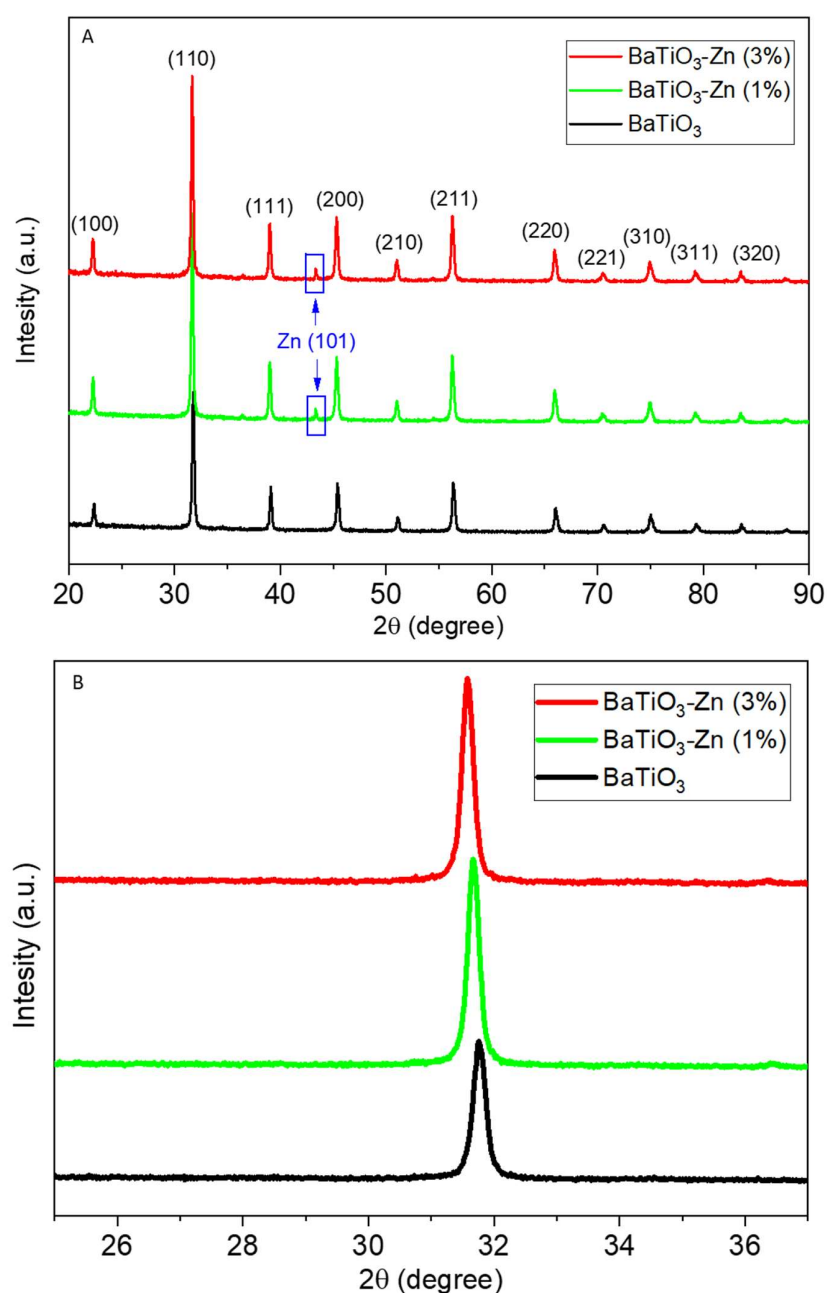


Figure 1. XRD spectra of pure and Zn-doped BaTiO₃ nanoparticles (A) and peak shifts (B).

2.2. Electron Microscopy Analysis

The microstructure, particle size, and morphology of pure BaTiO_3 and Zn-doped BaTiO_3 nanoparticles were analyzed via TEM and SEM. The particle size distribution obtained from the TEM images is presented in Figure 2A–C. The TEM micrographs depicted in Figure 2D–F serve as representations of the pure BaTiO_3 , 1% Zn– BaTiO_3 , and 3% Zn– BaTiO_3 nanoparticles, respectively. As we can see in the TEM images, the synthesized samples have a nearly spherical shape. Particle size is reduced by Zn doping without changing the shape. Based on TEM measurements, the average particle size (calculated from 100 particles) of pure BaTiO_3 , 1% Zn– BaTiO_3 , and 3% Zn– BaTiO_3 nanoparticles was determined to be 59.7, 51.3, and 38.5 nm, respectively. These findings are in accordance with the XRD estimations. The tetragonal phase of the prepared nanoparticles is confirmed by the visible lattice fringes observed in the high-resolution TEM images, as depicted in Figure 2G–I. The lattice's interplanar spacing was measured to be approximately 0.281–0.285 nm, corresponding to the interplanar distance of the (100) plane within the tetragonal phase of the BaTiO_3 nanostructure. The interplanar spacing of zinc (Zn) lattice fringes is observed in the range of 0.241–0.243 nm, indicating the presence of the cubic crystal structure of Zn with the (101) crystallographic plane. The lattice distances were found to be consistent with the XRD results.

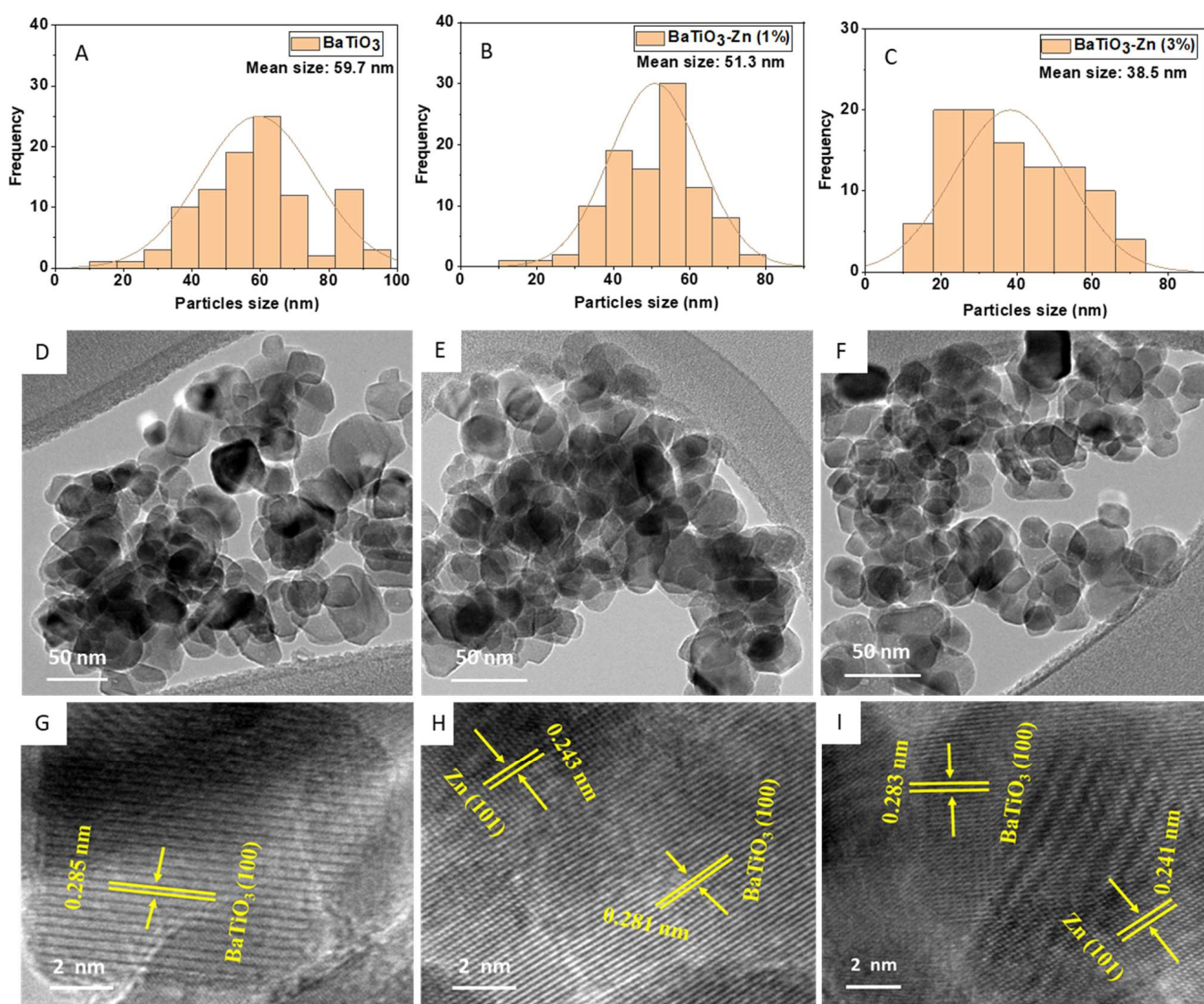


Figure 2. TEM particle size distribution (A–C), TEM micrographs of low (D–F) and high (G–I) resolutions of pure BaTiO_3 , 1% Zn– BaTiO_3 , and 3% Zn– BaTiO_3 nanoparticles, respectively.

The typical SEM images of nanostructures constructed of pure BaTiO₃, 1% Zn–BaTiO₃, and 3% Zn–BaTiO₃ are shown in Figure 3A–C, respectively. These images suggested the spherical form of nanoparticles, and it was found that the size of BaTiO₃ particles decreases with increasing Zn doping. According to SEM-coupled EDS analysis (Figure 3D), 3% Zn–BaTiO₃ included stoichiometric levels of Ba (68.46%), Ti (21.20%), O (7.64%), and Zn (2.71%). The SEM elemental mapping of 3% Zn–BaTiO₃ (Figure 4) provided additional confirmation of the presence of Zn, Ba, Ti, and O in the synthesized Zn-doped BaTiO₃ nanoparticles.

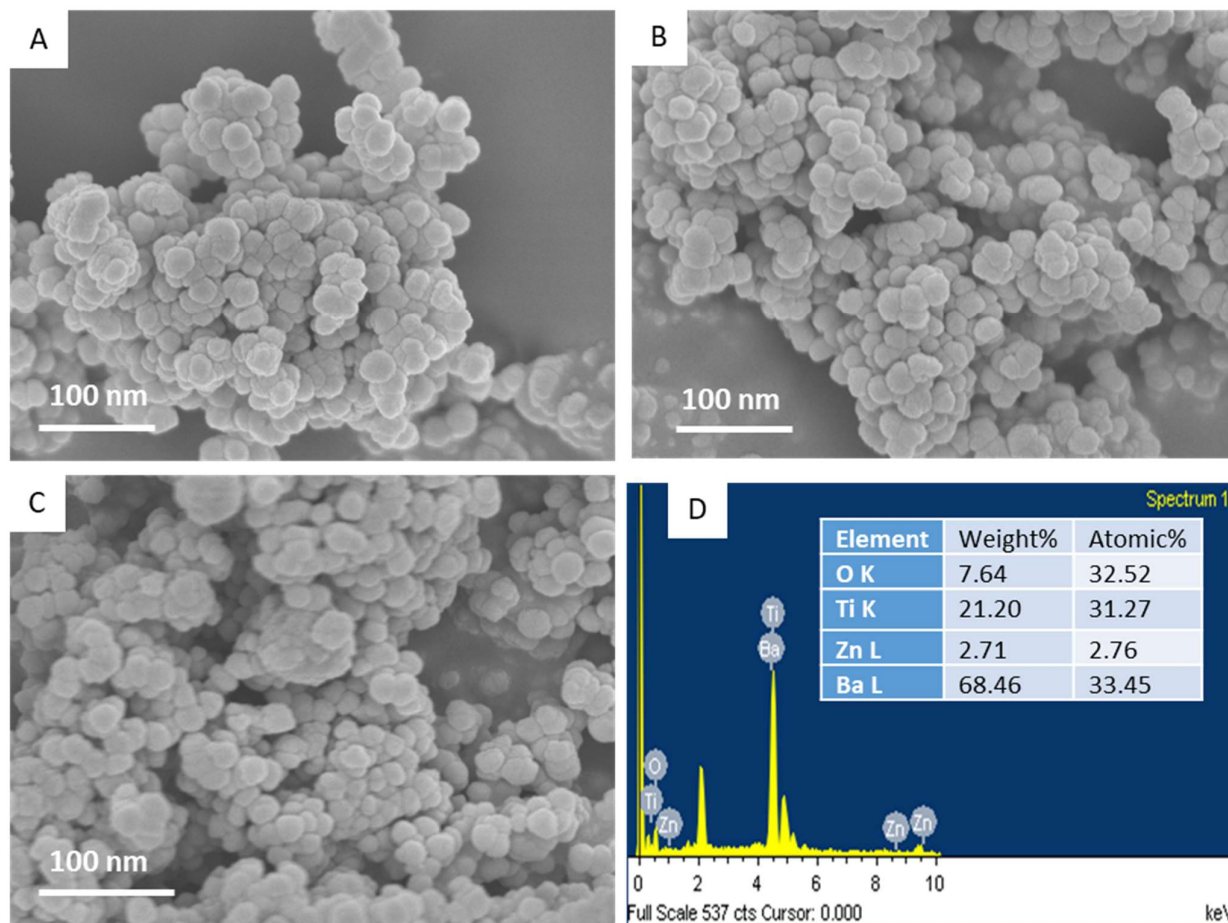


Figure 3. SEM micrographs of pure BaTiO₃ (A), 1% Zn–BaTiO₃ (B), and 3% Zn–BaTiO₃ (C) nanoparticles. (D) Elemental composition of 3% Zn–BaTiO₃ nanoparticles analyzed via EDS.

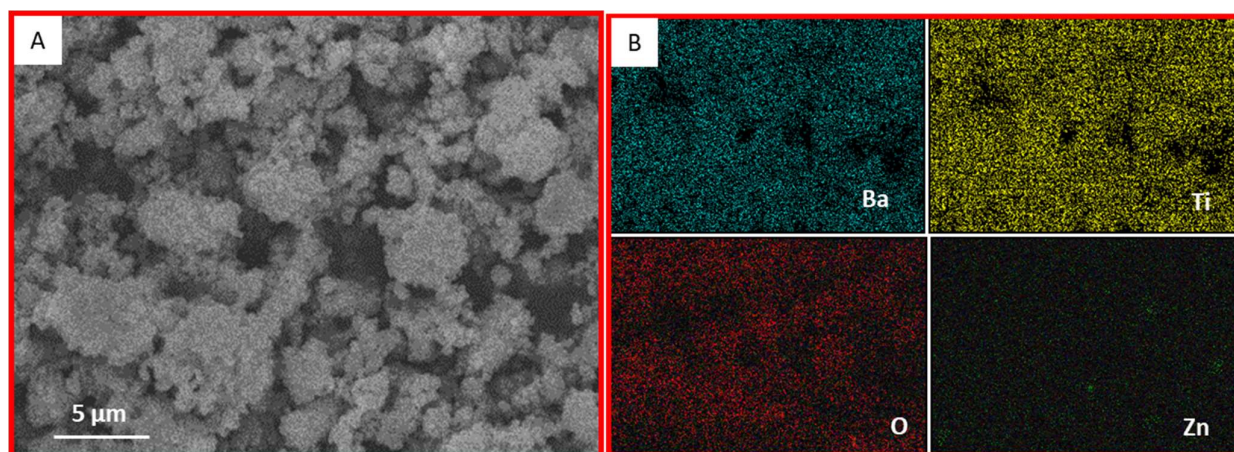


Figure 4. SEM micrograph (A) and elemental mapping (B) of 3% Zn–BaTiO₃ nanoparticles.

2.3. XPS Analysis

The surface chemical content of the prepared materials was analyzed using XPS. Figure 5A–E shows the XPS survey spectra of Zn-doped BaTiO₃ nanoparticles and the high-resolution signals of individual elements such as Ba 3d, Ti 2p, Zn 2p, and O 1s. The Ba 3d signal of the XPS spectra shows two bands, Ba 3d_{5/2} and Ba 3d_{3/2}, located at 781.9 eV and 797.1 eV, respectively (Figure 5B). The valence of Ti in BaTiO₃ nanoparticles was demonstrated by the Ti 2p signal, which had two peaks, Ti 2p_{3/2} and Ti 2p_{1/2}, at 460.9 eV and 466.2 eV, respectively (Figure 5C) [8]. The binding energies of Zn 2p_{3/2} and Zn 2p_{1/2} were observed to be in the XPS spectra of Zn 2p at 1021.98 eV and 1045.1 eV, respectively (Figure 5D). The differences in peak energies (24 eV) indicate that Zn mostly exists in the Zn²⁺ state [22]. As we can see in Figure 5E, O 1s is divided into two peaks that are present at about 529.73 eV and 530.71 eV, respectively. These two peaks of O 1s correspond to oxygen atoms in the forms of Ba-O-Ti and Ti-O-Ti [1].

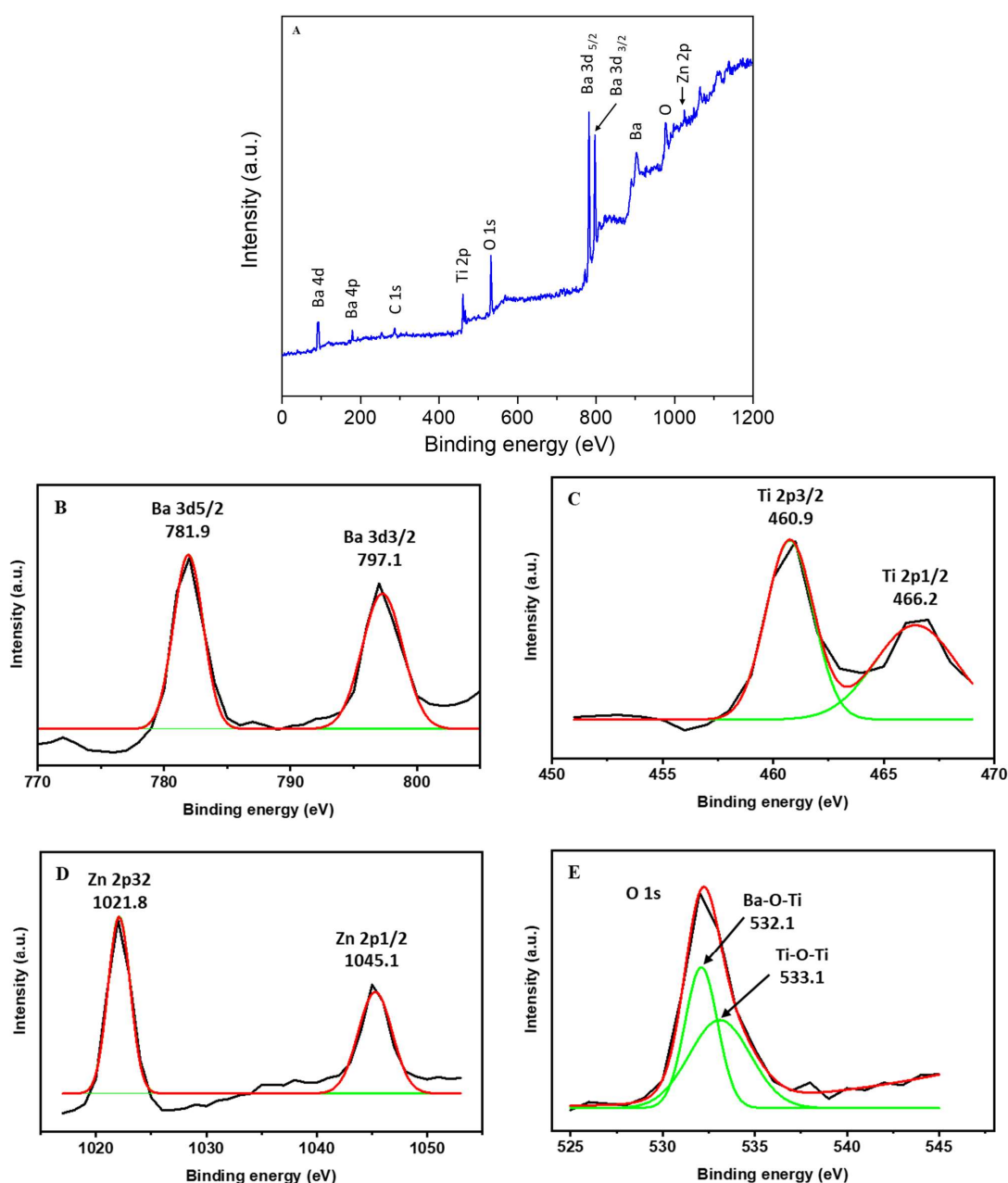


Figure 5. XPS survey spectrum of Zn (3%)-doped BaTiO₃ nanoparticles (A), high resolution signal of Ba 3d (B), Ti 2p (C), Zn 2p (D), and O 1s (E).

2.4. Brunauer–Emmett–Teller (BET) Analysis

The BET surface area and porosity of synthesized samples were assessed using the N_2 gas adsorption protocol. Figure 6A,B shows the adsorption–desorption isotherms and pore width distribution (insets) of pure and Zn (3%)-doped $BaTiO_3$ nanoparticles. These results suggest that both pure $BaTiO_3$ and Zn-doped $BaTiO_3$ nanoparticles exhibit a type IV pattern with a mesoporous nature per the IUPAC classification [3]. BET analysis shows that the surface area and pore size of Zn (3%)-doped $BaTiO_3$ nanoparticles were $14.4\text{ m}^2/\text{g}$ and 2.1 nm , which were different from those of pure $BaTiO_3$ nanoparticles ($9.3\text{ m}^2/\text{g}$ and 3.2 nm , respectively). In comparison to pure $BaTiO_3$ nanoparticles, the higher surface area and lower pore diameter of Zn (3%)-doped $BaTiO_3$ nanoparticles are beneficial for higher photocatalytic and anticancer effects [23].

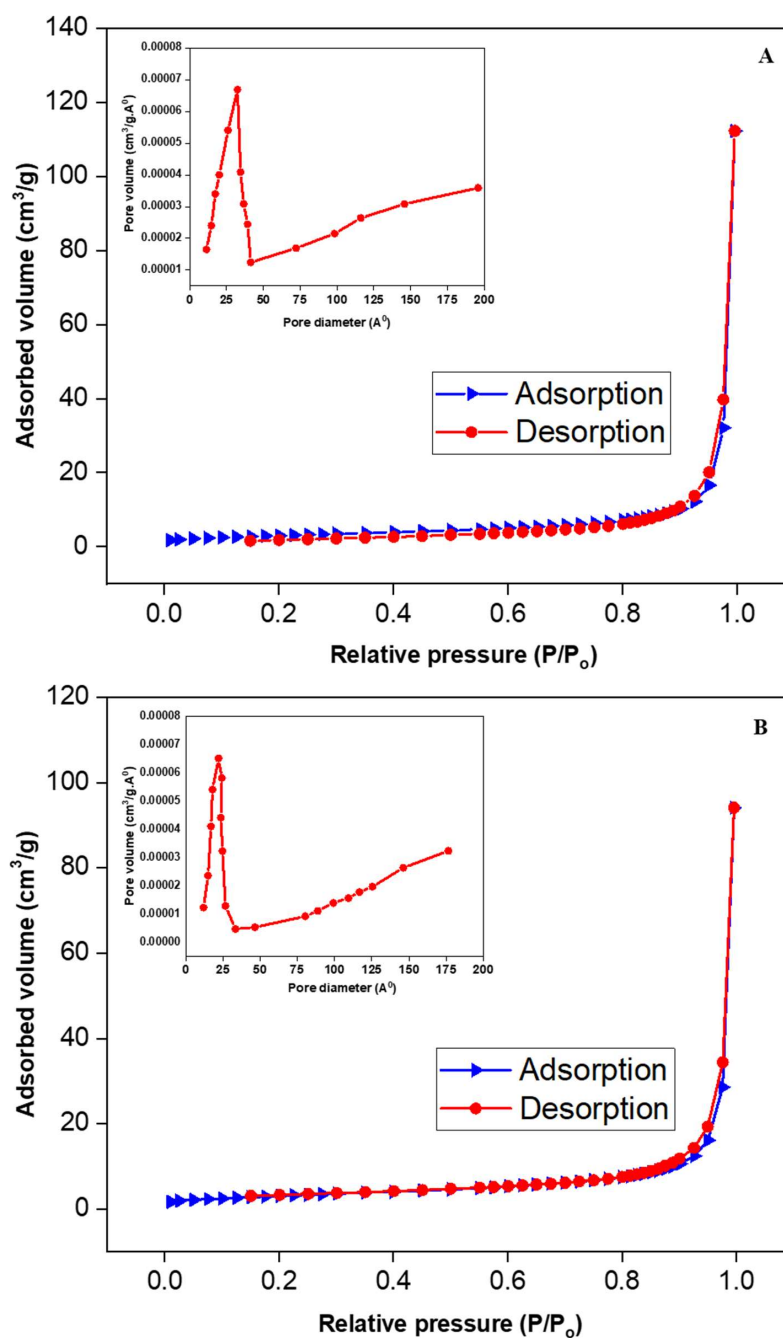


Figure 6. BET adsorption–desorption isotherms for pure $BaTiO_3$ (A) and Zn (3%)-doped $BaTiO_3$ nanoparticles (B). Insets represent the pore diameter distribution.

2.5. Raman Analysis

Raman spectroscopy was used to further assess the impact of Zn doping on the structural properties of BaTiO₃ nanoparticles. The range of wavenumbers of 200–1000 cm⁻¹ was evaluated in the room temperature Raman spectra of pure and Zn-doped BaTiO₃ nanoparticles (Figure 7). The major peaks of the tetragonal phase of BaTiO₃ were found at 306, 509, and 720 cm⁻¹ [24]. The peak at 306 cm⁻¹ was caused by the vibration of the TiO₆ group. Oxygen atom displacement was thought to be the source of the vibrations that caused the peak at 509 cm⁻¹. In addition, the ability to distinguish between the phase transition in pure BaTiO₃ and Zn-doped BaTiO₃ nanoparticles was facilitated by the appearance of a peak at 720 cm⁻¹, which could be attributed to the tetragonal phase of BaTiO₃. Furthermore, the strength of Raman peaks altered with increasing Zn doping, revealing that the higher the Zn doping, the lower the peak intensity. The tetragonal phase and decreased peak intensity of BaTiO₃ nanoparticles after Zn doping are desirable for enhanced photocatalytic and anticancer activity.

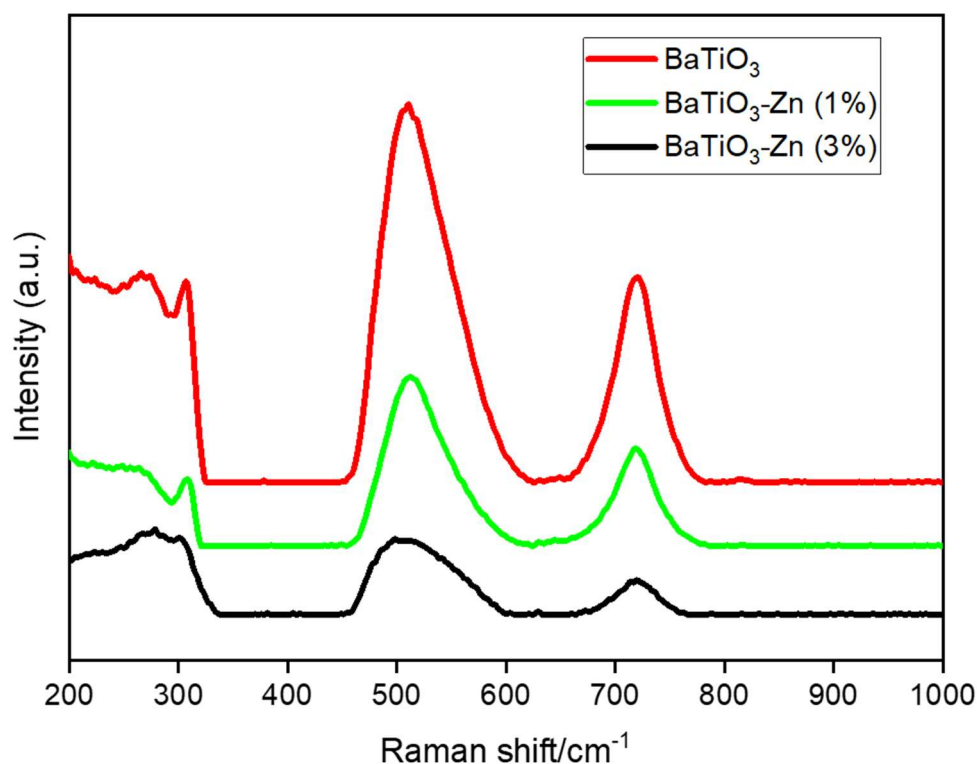


Figure 7. Raman spectroscopy of pure and Zn-doped BaTiO₃ nanoparticles.

2.6. Photoluminescence (PL) Analysis

Prepared nanoparticles were investigated using PL spectra to better comprehend the segregation of photogenerated charge carriers from their excited state. Pure BaTiO₃, 1% Zn–BaTiO₃, and 3% Zn–BaTiO₃ nanoparticles were excited at 350 nm, and their PL spectra were recorded at room temperature (Figure 5). In this case, the emission maxima of all three nanoparticles were located around 400 and 486 nm. The PL intensity of Zn-doped BaTiO₃ nanoparticles was lower compared to that of pure BaTiO₃ nanoparticles, and it reduced as the Zn concentration increased. The recombination rate of photogenerated electron–hole pairs is projected to be lower and the photocatalytic activity is projected to be higher at lower PL intensities [8]. Figure 8 shows that Zn (3%)-doped BaTiO₃ nanostructures effectively inhibit recombination between charge carriers because their peak intensity is lower than that of pure BaTiO₃ nanoparticles. Zn doping creates oxygen vacancies within the crystal lattice of BaTiO₃ nanoparticles due to the charge imbalance caused by the substitution of zinc ions with titanium or barium ions. The oxygen vacancies trapped the photo-induced

charge carriers (electrons/holes). This phenomenon enhances the generation of reactive oxygen species (ROS), leading to enhanced photocatalytic and anticancer activity.

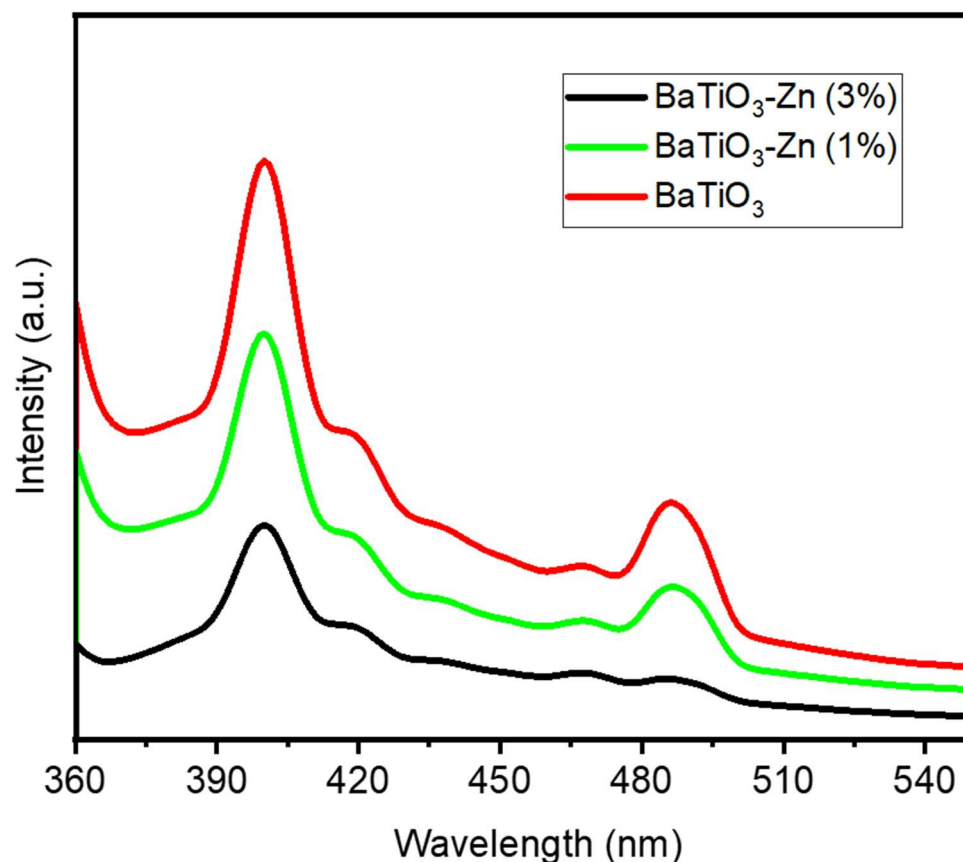


Figure 8. Photoluminescence spectra of pure and Zn-doped BaTiO₃ nanoparticles.

2.7. Photocatalytic Analysis

The photocatalytic activity of pure BaTiO₃ and Zn (1% and 3%)-doped BaTiO₃ nanoparticles was tested by watching how methylene blue (MB) dye degraded over time when exposed to visible light. The results are shown in Figure 9A–C. All of the synthesized nanoparticles had a MB absorption peak at 663 nm, which decreased with time and disappeared after around 80 min, suggesting that all of the MB molecules were digested. Based on the relation provided in the experimental section, the decomposition efficiency of nanoparticles was determined. Degradation profiles show that after 80 min of exposure to visible light, the pure BaTiO₃, 1% Zn–BaTiO₃, and 3% Zn–BaTiO₃ nanoparticles had photocatalytic activities of 58%, 70%, and 85%, respectively (Figure 9D). Zn-doped BaTiO₃ nanoparticles had a reduced electron–hole recombination rate, a smaller particle size, and a higher surface area, all of which contributed to their increased photocatalytic activity [8]. We also compare the organic pollutant degradation efficiency of Zn-doped BaTiO₃ nanoparticles with that found in earlier studies (Table 1).

Green-fabricated Zn-doped BaTiO₃ nanoparticles may have more potential for use if they are durable and can be used several times [12]. Five photodegradation cycles were performed under constant research circumstances to determine the reusability and stability of 3% Zn–BaTiO₃ nanoparticles. There was just a little drop in photocatalytic effectiveness from 85 to 83% after five test cycles. This demonstrates that the Zn-doped BaTiO₃ photocatalysts prepared from banana peel extract are reasonably stable when exposed to visible light, which is encouraging for their potential use in environmental remediation.

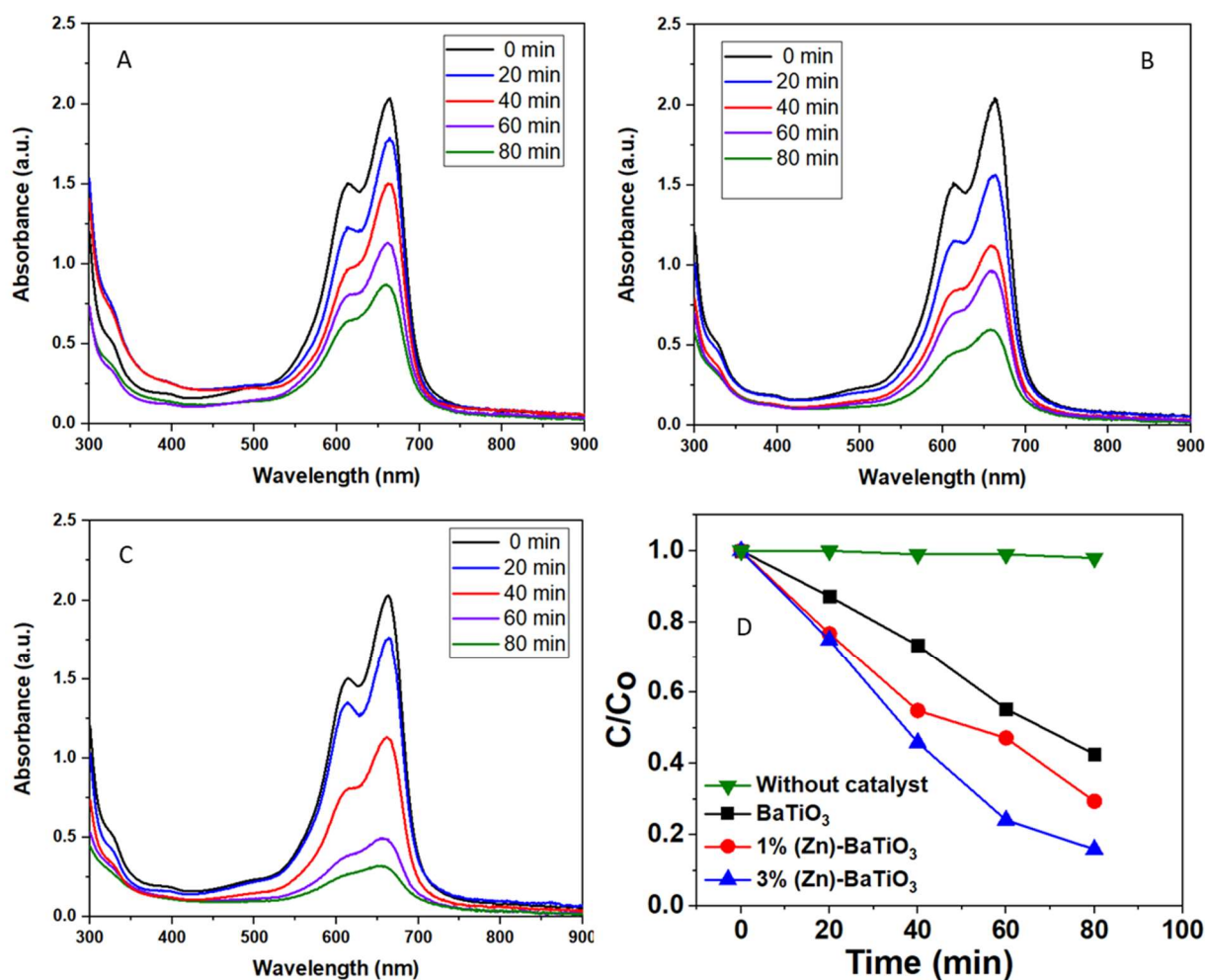


Figure 9. Time-dependent absorption spectra of MB dye solution under visible-light irradiation with pure BaTiO₃ (A), 1% Zn–BaTiO₃ (B), 3% Zn–BaTiO₃ (C), and photocatalytic degradation (C/C_0 versus time plot) of MB dye solution with the same nanoparticles (D).

Table 1. A comparison of the pollutant degradation efficiency of Zn-doped BaTiO₃ nanoparticles with that found in earlier studies.

Samples	Pollutants	Light Source	Exposure Time	Degradation Efficiency (%)	References
Zn–BaTiO ₃ nanoparticles	Methylene blue	Visible	80 min	85%	Present work
Cu–BaTiO ₃ nanoparticles	methyl violet	Visible	120 min	99%	[25]
Ag–BaTiO ₃ nanoparticles	Rhodamine B	UV	105 min	79%	[3]
Ag–BaTiO ₃ nanoparticles	Rhodamine B	UV	75 min	83%	[26]
BaTiO ₃ @rGO nanocomposites	Methylene blue	Visible	200 min	96%	[8]
BaTiO ₃ /γ–Al ₂ O ₃ composite	tetracycline hydrochloride	Visible	120 min	91%	[27]
Bi ₄ Ti ₃ O ₁₂ –BaTiO ₃ nanocomposite	Rhodamine B	Solar	60 min	43%	[28]

2.8. Anticancer Study

Currently, there is ongoing research into the potential application of semiconductor nanoparticles doped with metal ions in the field of cancer therapy [29,30]. Recent reports suggest that BaTiO₃ nanoparticles may have potential for use in biomedical applications, such as cancer treatment [6,31]. The impact of metal ion doping on the anticancer properties of BaTiO₃ has not been extensively studied. This study investigates the potential anticancer effect of pure and Zn-doped BaTiO₃ nanoparticles on human lung cancer cells

(A549). Cancer cells were exposed to varying concentrations (1–200 $\mu\text{g}/\text{mL}$) of pure BaTiO_3 , 1% Zn-BaTiO_3 , and 3% Zn-BaTiO_3 nanoparticles for 24 h. Anticancer activity was assessed using the MTT assay. The results depicted in Figure 10A indicate that both the pure and Zn-doped BaTiO_3 nanoparticles exhibited dose-dependent anticancer activity in cancer (A549) cells. Moreover, the anticancer efficacy of BaTiO_3 nanoparticles increases with increasing amounts of Zn doping. The inhibitory concentration (IC_{50}) of pure BaTiO_3 , 1% Zn-BaTiO_3 , and 3% Zn-BaTiO_3 nanoparticles was 64.4, 35.9, and 15.4 $\mu\text{g}/\text{mL}$, respectively. This finding indicates that the incorporation of Zn^{2+} ions is a significant factor in augmenting the anticancer efficacy of BaTiO_3 nanoparticles.

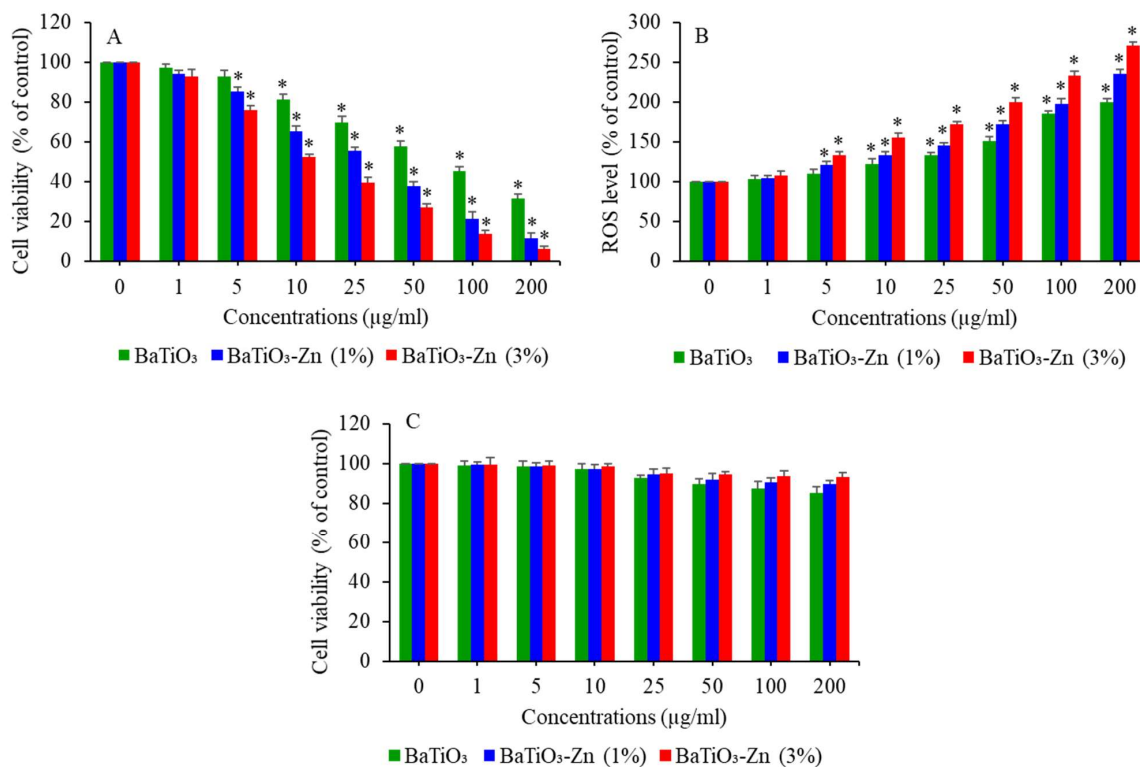


Figure 10. Anticancer activity (A) and ROS generation (B) of pure and Zn-doped BaTiO_3 nanoparticles in human lung cancer A549 cells. Cytocompatibility of the same nanoparticles in non-cancerous human lung fibroblasts (IMR90) (C). The results are shown as the mean and standard deviation of three separate experiments ($n = 3$). * denotes significant difference from the control ($p < 0.05$ level). GraphPad Prism (version 6.05) was used for the statistical analysis.

Semiconductor nanomaterials have been proposed to exhibit anticancer activity through the potential mechanism of ROS-induced oxidative stress [32,33]. Therefore, we investigated the intracellular level of ROS in the cancer (A549) cells after exposure to various concentrations (1–200 $\mu\text{g}/\text{mL}$) of pure BaTiO_3 , 1% Zn-BaTiO_3 , and 3% Zn-BaTiO_3 nanoparticles for 24 h. The results depicted in Figure 10B indicate that the prepared samples elicited a statistically significant, dose-dependent increase in ROS generation in cancer cells. Furthermore, when compared to pure BaTiO_3 nanoparticles, the Zn-doped BaTiO_3 nanoparticles exhibited a higher ROS level, and ROS generation increased with increasing the percentage of Zn dopant.

Zn doping creates several beneficial modifications in BaTiO_3 nanoparticles, which are highly beneficial for enhanced anticancer activity. Zn doping reduced particle size, increased surface area, and reduced the rate of electron/hole recombination in BaTiO_3 nanoparticles. This is a perfect setting for surface redox reactions that can cause cancer cells to produce ROS. Our results indicated that Zn-doped BaTiO_3 nanoparticles destroy cancer cells through ROS generation.

2.9. Cytocompatibility Study

The biocompatibility of possible anticancer agents should also be investigated in normal cells. This prompted us to assess the effect of pure and Zn-doped BaTiO₃ nanoparticles on normal lung fibroblasts (IMR90). Figure 10C showed that the normal IMR90 cells were not affected by either pure or Zn-doped BaTiO₃ nanoparticles. Interestingly, the cytocompatibility of BaTiO₃ nanoparticles improves with increasing the percentage of Zn doping. Overall, these results suggest that Zn-doped BaTiO₃ nanoparticles might destroy cancer cells while having minimal effect on healthy cells. Based on these findings, researchers may investigate the anticancer effects of Zn-BaTiO₃ nanoparticles in other human cancer cell lines and appropriate in vivo systems.

3. Materials and Methods

3.1. Preparation of Banana Peel Extract

Locally purchased ripped bananas were used to obtain the banana peels. Fruit peels were washed in deionized water and dried using a food dryer. Dried peels were ground into a powder using an electric grinder. The banana peel powder (10 g) was added to 500 mL of deionized water and stirred constantly for 6 h. After that, it was placed in a water bath at 60 °C for 1 h. The final step was to filter the mixture through filter paper (pore size 0.2 µm), and the filtrate (extract) was stored at 4 °C for further use in nanoparticle synthesis.

3.2. Eco-Friendly Production of Zn-Doped BaTiO₃ Nanoparticles

Banana peel extract, barium acetate, tetrabutyl titanate, and zinc acetate were used as precursors for the synthesis of Zn-doped BaTiO₃ nanoparticles. In brief, stoichiometric amounts of barium acetate, tetrabutyl titanate, and zinc acetate were initially dissolved in deionized water in individual flasks. These solutions were then added to the banana peel extract and stirred for 1 h. After that, the mixture was kept in a water bath at 60 °C for 12 h. In order to obtain Zn-doped BaTiO₃ nanostructures, the dried samples (1 g) were calcined at 900 °C for 5 h in a muffle furnace. A similar method was used to synthesize pure BaTiO₃ nanoparticles without the addition of zinc acetate. A graphical illustration of the green synthesis of Zn-doped BaTiO₃ nanoparticles is presented in Figure 11.

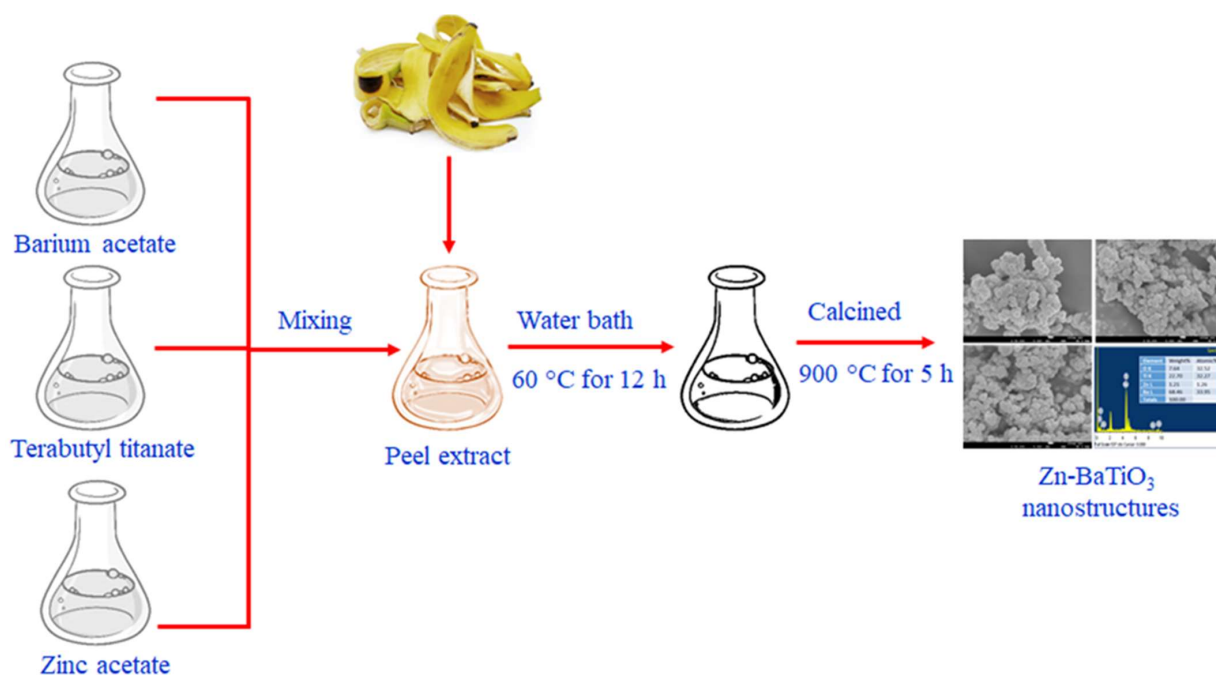


Figure 11. A graphical illustration of the green synthesis of Zn-doped BaTiO₃ nanoparticles from banana peel extract.

3.3. Characterization

XRD (PanAlytical X'pert Pro) was employed to characterize the crystallinity and phase purity of prepared nanoparticles. Shape, size, surface morphology, and elemental analysis were further determined via field emission scanning electron microscopy (FESEM, JSM-7600F, JEOL, Inc., Tokyo, Japan), field emission transmission electron microscopy (FETEM, JEM-2100, JEOL), and energy-dispersive X-ray spectroscopy (EDS). A fluorescence spectrophotometer (Hitachi F-4600) was used to record the luminescence spectra. XPS analysis was carried out in the ESCA system (VG 3000) with monochromatic MgK α (1253.6 eV) radiation. Raman spectroscopy was used to examine the existing phases of synthesized samples (Perkin-Elmer 400F) using a 514 nm laser beam. The specific surface area and pore size distribution were determined via BET analysis under nitrogen gas adsorption (Gemini VII 2390, Micromeritics).

3.4. Photocatalytic Evaluation

The degradation of methylene blue (MB) dye under visible-light irradiation was used to measure the photocatalytic activity of pure and Zn-doped BaTiO₃ nanoparticles. In 60 mL of the MB aqueous solution, the necessary amount of nanoparticles was added (the MB dye concentration in the aqueous solution without catalyst was 20 mg/L). Prior to exposure, the dye and nanoparticle suspensions were magnetically agitated for 90 min in the dark. The goal was to keep the dye and nanoparticles in equilibrium between adsorption and desorption. The resulting mixture was then poured into a 50 mL quartz test tube and exposed to visible light. A 400 W sodium lamp (Philips) in the 300–900 nm wavelength was used as a visible light source for the irradiation of solution. The ability of nanoparticles to degrade dye was observed by measuring the strength of the absorption peak at 663 nm. The degradation efficiency of nanoparticles was estimated using the equation photodegradation (%) = $[1 - (C/C_0)] \times 100\%$, where C₀ and C display the original concentration of the dye solution at the initial level and after a certain duration of light irradiation.

3.5. Biological Assays

Human lung cancer cells (A549) and their normal counterparts, lung fibroblast cells (IMR90), were employed for cytotoxicity studies. The cells were cultured in DMEM supplemented with 10% FBS, 100 U/mL penicillin, and 100 μ g/mL streptomycin. The cells were maintained in a humidified incubator at 37 °C with a 5% CO₂ supply. Cells were exposed to various concentrations (1–200 μ g/mL) of nanoparticles for 24 h. The cytotoxicity of nanoparticles in cancer and normal cells was investigated using an MTT assay with minor changes, as described earlier [34,35].

The ROS level in cancer cells following exposure to 1–200 μ g/mL nanoparticles for 24 h was determined using the probe 2,7-dichlorofluorescein diacetate (DCFH-DA). This is a cell-permeable nonfluorescent dye that is oxidized by ROS to produce highly fluorescent DCF [36]. Using a microplate reader (Synergy-HT, BioTek, Winooski, VT, USA), the fluorescence of DCF was measured at the 485/520 nm excitation/emission wavelength.

4. Conclusions

Banana peel extract was used to successfully synthesize pure and Zn-doped BaTiO₃ nanoparticles. The XRD, XPS, TEM, SEM, EDS, BET, Raman, and PL methods were used to characterize the as-synthesized samples. In XRD analysis, the tetragonal phase of BaTiO₃ was observed in all the prepared samples, and a new Zn peak was observed in the Zn-doped BaTiO₃. XRD, TEM, and SET data found that Zn doping decreased the particle size without changing the morphology of BaTiO₃. BET adsorption–desorption isotherms indicate that Zn doping increases the surface area of BaTiO₃ nanoparticles. The intensity of the PL spectra of BaTiO₃ decreased following Zn doping, indicating a declining recombination rate of electron–hole pairs. The degradation efficiency of pure BaTiO₃, 1% Zn–BaTiO₃, and 3% Zn–BaTiO₃ nanoparticles for MB dye under visible light was 58%, 70%, and 85%, respectively. In vitro studies demonstrated that Zn-doped BaTiO₃ nanoparticles were more effective than pure BaTiO₃ nanoparticles at killing human lung cancer (A549)

cells. Additionally, Zn-doped BaTiO₃ nanoparticles have high cytocompatibility in normal lung fibroblasts (IMR90) compared to pure BaTiO₃. The improved photocatalytic and anticancer activity of Zn–BaTiO₃ nanoparticles can be attributed to their reduced particle size, increased surface area, and reduced electron–hole recombination rates in comparison to those of pure BaTiO₃ nanoparticles. Further investigation into the photocatalytic activity and cancer fighting potential of green-fabricated Zn–BaTiO₃ nanoparticles is warranted. This research also underlines that agricultural waste (e.g., fruit peel) is useful for fabricating nanoparticles with potential environmental and therapeutic benefits.

Author Contributions: Conceptualization, supervision, funding acquisition, investigation and methodology, writing—original draft preparation, and writing—review and editing: M.A. Investigation and methodology, formal analysis, recourses, writing—review and editing, M.A.M.K. All authors have read and agreed to the published version of the manuscript.

Funding: The authors extend their sincere appreciation to the Researchers Supporting Project number (RSP2023R129), King Saud University, Riyadh, Saudi Arabia.

Data Availability Statement: The raw data will be available from corresponding author upon reasonable request.

Conflicts of Interest: The authors declare no conflict of interest.

References

1. Qi, J.; Li, Y.; Zhang, X.; Wang, J.; Zhang, Q.; Xue, Y.; Cheng, J.; Li, M.; Han, X.; Ma, Z.; et al. Solid-State Synthesis Semiconducting BaTiO₃ Nanoparticles at Low Temperature. *Mater. Chem. Phys.* **2020**, *242*, 122496. [[CrossRef](#)]
2. Jiang, B.; Iocozzia, J.; Zhao, L.; Zhang, H.; Harn, Y.W.; Chen, Y.; Lin, Z. Barium Titanate at the Nanoscale: Controlled Synthesis and Dielectric and Ferroelectric Properties. *Chem. Soc. Rev.* **2019**, *48*, 1194–1228. [[CrossRef](#)]
3. Khan, M.A.M.; Kumar, S.; Ahmed, J.; Ahamed, M.; Kumar, A. Influence of Silver Doping on the Structure, Optical and Photocatalytic Properties of Ag-Doped BaTiO₃ Ceramics. *Mater. Chem. Phys.* **2021**, *259*, 124058. [[CrossRef](#)]
4. Singh, M.; Yadav, B.C.; Ranjan, A.; Kaur, M.; Gupta, S.K. Synthesis and Characterization of Perovskite Barium Titanate Thin Film and Its Application as LPG Sensor. *Sens. Actuators B Chem.* **2017**, *241*, 1170–1178. [[CrossRef](#)]
5. Marino, A.; Almici, E.; Migliorin, S.; Tapeinos, C.; Battaglini, M.; Cappello, V.; Marchetti, M.; de Vito, G.; Cicchi, R.; Pavone, F.S.; et al. Piezoelectric Barium Titanate Nanostimulators for the Treatment of Glioblastoma Multiforme. *J. Colloid Interface Sci.* **2019**, *538*, 449–461. [[CrossRef](#)] [[PubMed](#)]
6. Sood, A.; Desseigne, M.; Dev, A.; Maurizi, L.; Kumar, A.; Millot, N.; Han, S.S. A Comprehensive Review on Barium Titanate Nanoparticles as a Persuasive Piezoelectric Material for Biomedical Applications: Prospects and Challenges. *Small* **2023**, *19*, 2206401. [[CrossRef](#)]
7. Luo, B.; Wang, X.; Tian, E.; Li, G.; Li, L. Electronic Structure, Optical and Dielectric Properties of BaTiO₃/CaTiO₃/SrTiO₃ Ferroelectric Superlattices from First-Principles Calculations. *J. Mater. Chem. C* **2015**, *3*, 8625. [[CrossRef](#)]
8. Khan, M.A.M.; Kumar, S.; Ahamed, M.; Ahmed, J.; Kumar, A.; Shar, M.A. BaTiO₃@rGO Nanocomposite: Enhanced Photocatalytic Activity as Well as Improved Electrode Performance. *J. Mater. Sci. Mater. Electron.* **2021**, *32*, 12911–12921. [[CrossRef](#)]
9. Xie, L.; Hao, J.G.; Chen, H.Q.; Li, Z.X.; Ge, S.Y.; Mi, Y.; Yang, K.; Lu, K.Q. Recent Advances of Nickel Hydroxide-Based Cocatalysts in Heterogeneous Photocatalysis. *Catal. Commun.* **2022**, *162*, 106371. [[CrossRef](#)]
10. Tihiti, M.; Ibrahim, J.E.F.M.; Basyooni, M.A.; En-Nadir, R.; Belaid, W.; Hussainova, I.; Kocserha, I. Development of Yttrium-Doped BaTiO₃ for Next-Generation Multilayer Ceramic Capacitors. *ACS Omega* **2023**, *8*, 8448–8460. [[CrossRef](#)]
11. Chakraborty, T.; Mukherjee, S.; Mukherjee, S. Effect of Zn Doping on the Crystallization, Dielectric, and Ferroelectric Properties of Solid State Sintered Barium Stannate. *InterCeram Int. Ceram. Rev.* **2017**, *66*, 101–110. [[CrossRef](#)]
12. Arunkumar, D.R.; Anjelin Ursula Portia, S.; Ramamoorthy, K. Design and Fabrication of Novel Tb Doped BaTiO₃ Thin Film with Superior Light-Harvesting Characteristics for Dye Sensitized Solar Cells. *Surf. Interfaces* **2021**, *22*, 100853. [[CrossRef](#)]
13. Singh, J.; Dutta, T.; Kim, K.H.; Rawat, M.; Samddar, P.; Kumar, P. “Green” Synthesis of Metals and Their Oxide Nanoparticles: Applications for Environmental Remediation. *J. Nanobiotechnol.* **2018**, *16*, 84. [[CrossRef](#)] [[PubMed](#)]
14. Behzad, F.; Naghib, S.M.; Kouhbanani, M.A.J.; Tabatabaei, S.N.; Zare, Y.; Rhee, K.Y. An Overview of the Plant-Mediated Green Synthesis of Noble Metal Nanoparticles for Antibacterial Applications. *J. Ind. Eng. Chem.* **2021**, *94*, 92–104. [[CrossRef](#)]
15. Kalpana, V.N.; Devi Rajeswari, V. A Review on Green Synthesis, Biomedical Applications, and Toxicity Studies of ZnO NPs. *Bioinorg. Chem. Appl.* **2018**, *2018*, 3569758. [[CrossRef](#)]
16. Mohd Zaini, H.; Roslan, J.; Saallah, S.; Munsu, E.; Sulaiman, N.S.; Pindi, W. Banana Peels as a Bioactive Ingredient and Its Potential Application in the Food Industry. *J. Funct. Foods* **2022**, *92*, 105054. [[CrossRef](#)]
17. Ruangtong, J.; Jiraroj, T.; T-Thienprasert, N.P. Green Synthesized ZnO Nanosheets from Banana Peel Extract Possess Anti-Bacterial Activity and Anti-Cancer Activity. *Mater. Today Commun.* **2020**, *24*, 101224. [[CrossRef](#)]

18. Goh, H.T.; Cheok, C.Y.; Yeap, S.P. Green Synthesis of Silver Nanoparticles Using Banana Peel Extract and Application on Banana Preservation. *Food Front.* **2023**, *4*, 283–288. [[CrossRef](#)]
19. Ahamed, M.; Khan, M.A.M.; Akhtar, M.J.; Alhadlaq, H.A.; Alshamsan, A. Role of Zn Doping in Oxidative Stress Mediated Cytotoxicity of TiO₂ Nanoparticles in Human Breast Cancer MCF-7 Cells. *Sci. Rep.* **2016**, *6*, 30196. [[CrossRef](#)]
20. Patterson, A.L. The Scherrer Formula for X-ray Particle Size Determination. *Phys. Rev.* **1939**, *56*, 978–982. [[CrossRef](#)]
21. Ahamed, M.; Akhtar, M.J.; Khan, M.A.M.; Alaizeri, Z.M.; Alhadlaq, H. Facile Synthesis of Zn-Doped Bi₂O₃ nanoparticles and Their Selective Cytotoxicity toward Cancer Cells. *ACS Omega* **2021**, *6*, 17353–17361. [[CrossRef](#)] [[PubMed](#)]
22. Narasimman, S.; Balakrishnan, L.; Alex, Z.C. Fiber Optic Magnetic Field Sensor Using Co Doped ZnO Nanorods as Cladding. *RSC Adv.* **2018**, *8*, 18243–18251. [[CrossRef](#)] [[PubMed](#)]
23. Bhat, D.K.; Bantawal, H.; Shenoy, U.S. Rhodium Doping Augments Photocatalytic Activity of Barium Titanate: Effect of Electronic Structure Engineering. *Nanoscale Adv.* **2020**, *2*, 5688–5698. [[CrossRef](#)] [[PubMed](#)]
24. Hayashi, H.; Nakamura, T.; Ebina, T. In-Situ Raman Spectroscopy of BaTiO₃ Particles for Tetragonal–Cubic Transformation. *J. Phys. Chem. Solids* **2013**, *74*, 957–962. [[CrossRef](#)]
25. Uma, P.I.; Shenoy, U.S.; Bhat, D.K. Electronic Structure Engineering of BaTiO₃ Cuboctahedrons by Doping Copper to Enhance the Photocatalytic Activity for Environmental Remediation. *J. Alloys Compd.* **2023**, *948*, 169600. [[CrossRef](#)]
26. Xu, S.; Liu, Z.; Zhang, M.; Guo, L. Piezotronics Enhanced Photocatalytic Activities of Ag-BaTiO₃ Plasmonic Photocatalysts. *J. Alloys Compd.* **2019**, *801*, 483–488. [[CrossRef](#)]
27. Yu, C.; Wang, S.; Zhang, K.; Li, M.; Gao, H.; Zhang, J.; Yang, H.; Hu, L.; Jagadeesha, A.V.; Li, D. Visible-Light-Enhanced Photocatalytic Activity of BaTiO₃/γ-Al₂O₃ Composite Photocatalysts for Photodegradation of Tetracycline Hydrochloride. *Opt. Mater.* **2023**, *135*, 113364. [[CrossRef](#)]
28. Singh, S.; Kumar, A.; Pandey, S.K.; Kumar, V.; Verma, M.K.; Gupta, A.; Mandal, K.D. Synthesis of Bi₄Ti₃O₁₂-BaTiO₃ Nanocomposite, Manifesting High Dielectric and Unique Magnetic Nature Applicable in Heterogeneous Photocatalytic Activity for Degradation of Rhodamine B Dye. *Mater. Technol.* **2020**, *36*, 476–491. [[CrossRef](#)]
29. Nagajyothi, P.C.; Muthuraman, P.; Tettey, C.O.; Yoo, K.; Shim, J. In Vitro Anticancer Activity of Eco-Friendly Synthesized ZnO/Ag Nanocomposites. *Ceram. Int.* **2021**, *47*, 34940–34948. [[CrossRef](#)]
30. Rajendran, R.; Mani, A. Photocatalytic, Antibacterial and Anticancer Activity of Silver-Doped Zinc Oxide Nanoparticles. *J. Saudi Chem. Soc.* **2020**, *24*, 1010–1024. [[CrossRef](#)]
31. Ahamed, M.; Akhtar, M.J.; Majeed Khan, M.A.; Alhadlaq, H.A.; Alshamsan, A. Barium Titanate (BaTiO₃) Nanoparticles Exert Cytotoxicity through Oxidative Stress in Human Lung Carcinoma (A549) Cells. *Nanomaterials* **2020**, *10*, 2309. [[CrossRef](#)] [[PubMed](#)]
32. Prashanth, G.K.; Prashanth, P.A.; Singh, P.; Nagabhushana, B.M.; Shivakumara, C.; Krishnaiah, G.M.; Nagendra, H.G.; Sathyananda, H.M.; Chaturvedi, V. Effect of Doping (with Cobalt or Nickel) and UV Exposure on the Antibacterial, Anticancer, and ROS Generation Activities of Zinc Oxide Nanoparticles. *J. Asian Ceram. Soc.* **2020**, *8*, 1175–1187. [[CrossRef](#)]
33. Ciccacese, F.; Raimondi, V.; Sharova, E.; Silic-Benussi, M.; Ciminale, V. Nanoparticles as Tools to Target Redox Homeostasis in Cancer Cells. *Antioxidants* **2020**, *9*, 211. [[CrossRef](#)] [[PubMed](#)]
34. Mosmann, T. Rapid Colorimetric Assay for Cellular Growth and Survival: Application to Proliferation and Cytotoxicity Assays. *J. Immunol. Methods* **1983**, *65*, 55–63. [[CrossRef](#)]
35. Ahamed, M.; Javed Akhtar, M.; Majeed Khan, M.A.; Alhadlaq, H.A. Facile Green Synthesis of ZnO-RGO Nanocomposites with Enhanced Anticancer Efficacy. *Methods* **2022**, *199*, 28–36. [[CrossRef](#)]
36. Ahamed, M.; Lateef, R.; Akhtar, M.J.; Rajanahalli, P. Dietary Antioxidant Curcumin Mitigates CuO Nanoparticle-Induced Cytotoxicity through the Oxidative Stress Pathway in Human Placental Cells. *Molecules* **2022**, *27*, 7378. [[CrossRef](#)]

Disclaimer/Publisher’s Note: The statements, opinions and data contained in all publications are solely those of the individual author(s) and contributor(s) and not of MDPI and/or the editor(s). MDPI and/or the editor(s) disclaim responsibility for any injury to people or property resulting from any ideas, methods, instructions or products referred to in the content.